

# Angular distributions and angular momentum alignment of $O(^3P_J)$ atoms formed in the photolysis of $O_2$ via the Herzberg continuum

Dmitri Chestakov, Wim J. van der Zande, David H. Parker\*

*Institute for Molecules and Materials, Radboud University Nijmegen, Heyendaalsweg 135,  
6525 AJ, Nijmegen, The Netherlands*

Claire Vallance\*

*Department of Chemistry, University of Oxford,  
Chemistry Research Laboratory, 12 Mansfield Rd, Oxford OX1 3TA, UK*

\*corresponding authors: parker@science.ru.nl, claire.vallance@chem.ox.ac.uk

## Abstract

Sliced velocity-map imaging has been used to measure photofragment scattering distributions for the  $O(^3P_2)$  and  $O(^3P_1)$  products of  $O_2$  photolysis following laser excitation into the Herzberg continuum between 205 and 241 nm. The images have been analysed to extract the photofragment spatial anisotropy parameter,  $\beta$ , together with the alignment parameters  $a_0^{(2)}(\parallel)$ ,  $a_0^{(2)}(\perp)$ ,  $a_2^{(2)}(\perp)$ , and  $\text{Re}[a_1^{(2)}(\parallel, \perp)]$ . Our alignment measurements bridge the gap between the recent 193 nm measurement of Brouard *et al* [1] and those of Alexander *et al* [2] at 222 and 237 nm, and extend out to threshold at 241 nm. Our measured parameters show no strong dependence on photolysis wavelength. Near threshold we are able to separate the contributions from the  $O(^3P_2) + O(^3P_2)$  and  $O(^3P_2) + O(^3P_1)$  channels, and find significantly different photofragment alignments for the two cases.

# 1 Introduction

Atomic oxygen is an abundant species in the earth's atmosphere over a wide range of altitudes from 170 to 700 km [3], and is intimately involved in atmospheric photochemistry. The primary source of atomic oxygen in the atmosphere is photolysis of  $O_2$  following the absorption of solar radiation. The electronic structure of the  $O_2$  molecule is highly complex: two oxygen atoms in their  $^3P_J$  ground state give rise to a total of 81 possible molecular electronic states, with further molecular states correlating with excited state photofragments. Nonetheless, the large number of studies carried out on the  $O_2$  molecule have brought us some way towards a complete understanding of its UV photochemistry. Some of the low-lying electronic states of  $O_2$ , together with its UV absorption spectrum, are shown in Figure 1.

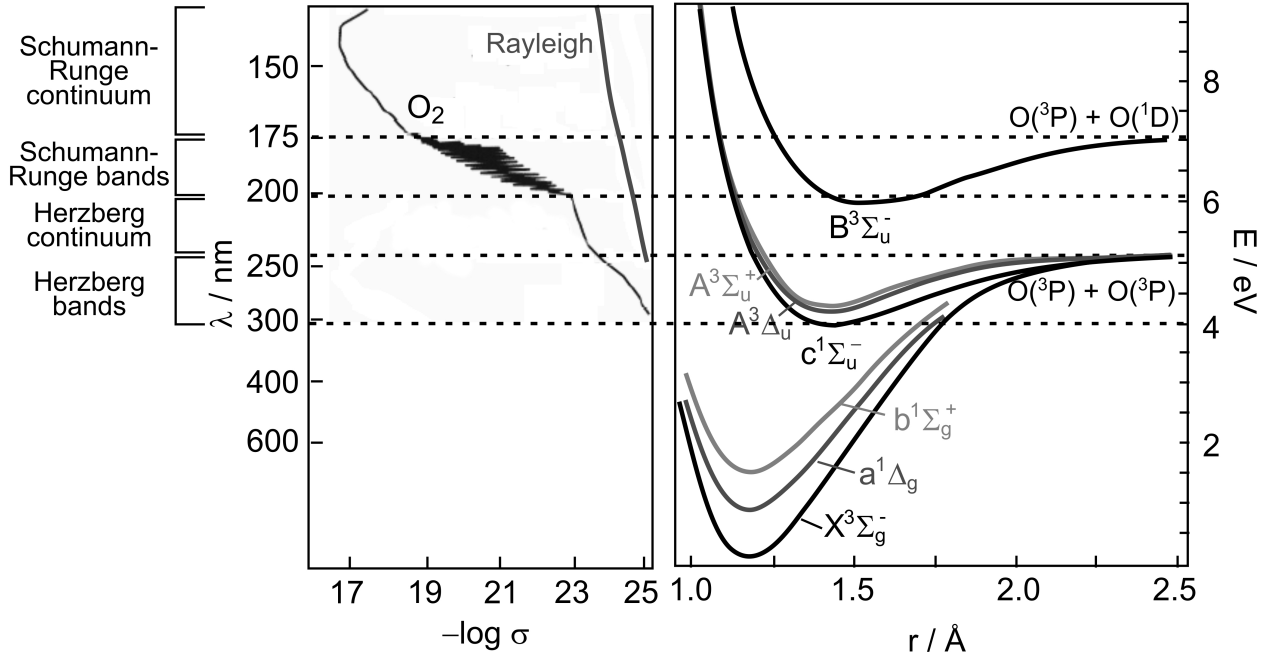


Figure 1: *Low lying electronic states and UV absorption spectrum of  $O_2$ .*

As is apparent from the absorption spectrum shown in Figure 1, UV excitation from the  $X(^3\Sigma_g^-)$  ground state of molecular oxygen can be separated into a number of distinct regions. Between 300 and 242 nm, excitation is into the  $A(^3\Sigma_u^+)$ ,  $c(^1\Sigma_u^-)$  and  $A'(^3\Delta_u)$  states.

These are forbidden transitions known as the Herzberg I, II and III bands, which gain oscillator strength via spin-orbit and orbit-rotation interactions with higher states. Below 242 nm we reach the threshold for dissociation to  $O(^3P) + O(^3P)$  products. The Herzberg continua have very small absorption cross sections, but the high number density of molecular oxygen at lower altitudes and the long path length through the atmosphere makes photolysis at these wavelengths an important atmospheric process; around 90% of atomic oxygen in the lower stratosphere is formed via the Herzberg states. Below 203 nm there is sufficient energy to access the  $B(^3\Sigma_u^-)$  state. This is the first fully allowed transition in molecular oxygen and constitutes the Schumann-Runge band system. The absorption cross section in the Schumann-Runge bands is large, and increases rapidly with decreasing wavelength. Predissociation within this band system leads to  $O(^3P) + O(^3P)$  photofragments. At 174 nm the threshold for production of  $O(^1D)$  is reached, and fragmentation to  $O(^1D) + O(^3P)$  dominates at wavelengths below this threshold. Higher states become involved below 130 nm, leading to more complex structure in the absorption spectrum.

The present study focuses on photolysis of  $O_2$  within the Herzberg continuum between 241 and 205 nm. The dynamics of  $O_2$  dissociation in this region have been the subject of a number of studies, most recently a series of theoretical investigations by van Vroonhoven and Groenenboom [4, 5], and experimental studies by Tonokura *et al* [6], Buijsse *et al* [7] and Alexander *et al* [2]. In addition, Brouard *et al* [1] and Bakker and Parker [8] have carried out stereodynamics studies at 193 nm, where dissociation via the Herzberg continua still contributes to the dynamics.

The key parameters measured in a dynamics study on a diatomic molecule are the product angular distribution, characterised by the anisotropy parameter,  $\beta$ , and the spatial distribution or ‘polarisation’ of the product electronic angular momentum. In the case of  $O_2$  dissociation via the Herzberg continuum, the fine-structure ( $J$  state) distribution also yields valuable information. The  $\beta$  parameter quantifies the extent of parallel and perpendicular character for the initial electronic excitation, and can therefore often reveal the identity of the initially excited state. In some photodissociation systems, the molecule will dissociate

on the initially excited state, but in many cases one or more curve crossings are involved. The fine-structure branching ratios and angular momentum alignment contain information on the final dissociating state and therefore on the extent of non-adiabaticity in the dissociation. This is often quantified by an adiabaticity parameter (sometimes called the Massey parameter)

$$\xi = \frac{\Delta R \Delta E_{\text{SO}}}{\hbar v} \quad (1)$$

The adiabaticity parameter simply compares the timescale of photofragment recoil,  $\Delta R/v$ , where  $\Delta R$  is a characteristic distance over which the fragments recoil before they can be considered as separate atoms and  $v$  is the recoil velocity, with the timescale of spin-orbit coupling,  $\hbar/\Delta E_{\text{SO}}$ , where  $E_{\text{SO}}$  is the spin-orbit coupling energy. At high recoil velocities,  $\xi \rightarrow 0$ , and we have the *sudden recoil* or *diabatic* limit. In this regime the molecular eigenstate is simply projected onto the atomic wavefunctions, and the atomic fine-structure distribution is close to statistical, with a  $2J + 1$  weighting to each component. At the other extreme of low recoil velocity, the Massey parameter tends to infinity and we have the adiabatic limit. The  $\Omega$  quantum number, defining the projection of  $\mathbf{J}$  onto the internuclear axis, is conserved during the dissociation, and remains a good quantum number even as we move from a Hund's case *a* regime in which  $\mathbf{L}$  and  $\mathbf{S}$  are coupled to the axis to a Hund's case *c* regime in which coupling between  $\mathbf{L}$  and  $\mathbf{S}$  dominates. In this case an adiabatic correlation diagram can be used to determine which atomic fine structure state correlates with the molecular fine structure state. This treatment ignores any couplings between the non-crossing case *c* potential energy curves. In most cases the situation will be intermediate between these two limits, and accurate potential energy surfaces and couplings between them are needed in order to predict the dynamics.

In the case of  $\text{O}_2$  dissociation in the Herzberg region, such data has been provided by the theoretical work of van Vroonhoven and Groenenboom, and has formed a basis for the interpretation of all subsequent experimental data. The first contribution of van Vroonhoven and Groenenboom was to carry out high level *ab initio* calculations of the potential energy curves for the eight electronically excited ungerade states of molecular oxygen correlating

with the  $O(^3P) + O(^3P)$  dissociation limit, together with the separation-dependent spin-orbit and radial derivative couplings between the states [4]. In a second paper [5], the potential energy curves were used to calculate wavelength-dependent branching ratios into the three fine structure ( $J$ ) components for the  $O(^3P_J)$  products, together with atomic polarisations and  $\beta$  parameters as a function of  $J$ . The calculations were carried out using a semi-classical model, and were compared with the results expected from the two limiting cases of purely diabatic or purely adiabatic behaviour. While the semiclassical model involves approximations, in the absence of a fully quantum treatment of the dissociation dynamics of  $O_2$ , it currently represents the best available theoretical data for comparison with experiment.

There have been three measurements of the  $O(^3P)$  fine structure branching ratio, all performed at a wavelength of 226 nm, and all in good agreement with each other within experimental errors. Tonokura *et al* [6] measured a  $J=0:1:2$  ratio of (1.0):(3.8):(9.6); Buijsse *et al* [7] measured (1.0):(3.3):(9.0); and Alexander *et al* [2] recorded a result of (1.0):(2.90):(8.65). In the adiabatic limit, the A, A' and c states correlate with the  $O(^3P_2) + O(^3P_2)$  limit, so the measured population in  $J = 1$  and  $J = 0$  implies a significant degree of non-adiabaticity during the dissociation. This is backed up by the calculations of Van Vroonhoven and Groenenboom, whose semi-classical model predicted a ratio of (1.0):(4.3):(9.7) at 226 nm, in good agreement with experiment. Neither the fully diabatic or fully adiabatic models could reproduce the experimental results.

Spatial anisotropy parameters were also recorded in all of the experimental studies described above, and for the most part are in good agreement<sup>1</sup>. Over the wavelength range from 193 nm to 226 nm,  $\beta$  appears stays fairly constant at a value of 0.5 to 0.6 for both the  $J = 1$  and  $J = 2$  photofragments. At 236 nm, near the threshold for dissociation,  $\beta$  for the

---

<sup>1</sup>Tonokura *et al* obtained an anomalously high value of  $\beta = 1.61$  at 193 nm from an analysis of photofragment Doppler profiles. This value is out of line with all other measurements of  $\beta$  at similar wavelengths, and may be a result of neglect of a two-photon photolysis contribution to the signal. Such contributions are clearly seen in the later velocity-map imaging measurements of Buijsse *et al*, but would yield a less obvious broad background in Doppler profile measurements.

$J = 1$  products reduces somewhat to around 0.25. No such reduction is apparent for the  $J = 2$  products. Buijsse *et al* [7] were also able to make measurements for the  $J = 0$  products at 204 and 226 nm, and obtained significantly lower  $\beta$  parameters of 0.35 and 0.37 at the two wavelengths. The first and most obvious conclusion from all of these measurements is that  $O_2$  dissociation via the Herzberg continuum takes place via a mixed parallel/perpendicular transition. For example, a  $\beta$  parameter of 0.612, as measured by Alexander *et al* at 226 nm, corresponds to a transition with 54% parallel and 46% perpendicular character. The transitions to the  $c(^1\Sigma_u^-)$  and  $A'(^3\Delta_u)$  states and to the  $(^3\Sigma_{u,0}^+)$  component of the A state are known to be perpendicular in character, while that to the  $^3\Sigma_{u,\pm 1}^+$  component of the A state is parallel in character. Buijsse *et al* used known transition moments and oscillator strengths from the literature [9, 10], together with their measured values for  $\beta$  to determine the contributions from each of the three Herzberg states, A, A' and c. The initial excitation leading to dissociation was found to be dominated by the Herzberg I transition involving the A state, with a contribution of 91% from this transition at 226 nm and 100% at 204 nm.

Angular momentum alignment has been measured at 222 and 237 nm in the study by Alexander *et al* [2] and at 193 nm by Brouard *et al* [1]. We leave a full discussion of this aspect of the dissociation dynamics to the Results and Discussion section.

In the following, we expand on the work described above by presenting the results of a sliced velocity-map imaging study into the photodissociation dynamics of  $O_2$  at seven different wavelengths spanning the Herzberg continuum, from threshold at 241 nm down to 205 nm.

## 2 Methods

The experiments were carried out using sliced velocity-map imaging, which records a central ‘slice’ through the full Newton sphere of recoiling atomic fragments, obviating the need for Abel inversion or other image reconstruction techniques.

The experimental setup is shown schematically in Figure 2. A pulsed source creates a

molecular beam of 5% O<sub>2</sub> seeded in argon, which travels along the axis of the instrument. After passing through a 2 mm skimmer, the beam enters the velocity mapping ion lens system, where it is intersected at right angles by counterpropagating photolysis and probe laser beams. The photolysis and probe lasers are both Nd:YAG-pumped tuneable dye systems (Spectra Physics PDL-2 dye lasers each pumped by a Continuum Surelite III Nd:Yag) with a pulse duration of around 6 ns. The photolysis laser provides tuneable radiation over the range from 200-242 nm with a pulse energy of 0.1-0.2 mJ, and the probe laser is tuned to (2+1)REMPI transitions of the O(<sup>3</sup>P<sub>2</sub>) and O(<sup>3</sup>P<sub>1</sub>) photofragments at 225.65 nm and 226.06 nm, respectively, with a pulse energy of around 0.3 mJ. The probe laser is focussed into the interaction region by a 25 cm lens.

The photolysis laser dissociates O<sub>2</sub> molecules in the molecular beam, forming O(<sup>3</sup>P) products that recoil with a fixed kinetic energy. After a short delay of 10-20 ns, the probe laser ionizes either the O(<sup>3</sup>P<sub>1</sub>) or O(<sup>3</sup>P<sub>2</sub>) fragments via (2+1)REMPI. Signal levels were not sufficient to record data for the O(<sup>3</sup>P<sub>0</sub>) fragment. After ionization, the Newton spheres of atomic photofragments continue to expand from the interaction region under essentially field-free conditions. After allowing the ion cloud to expand for 1.5  $\mu$ s, the velocity-mapping potentials are applied to the ion lens electrodes and the ions are accelerated towards a 2D position-sensitive detector. The detector consists of a pair of microchannel plates (MCPs), a phosphor screen, and a CCD (charge-coupled device) camera. The MCPs are time-gated using a home-built high-voltage pulse supply with a pulse width of  $\sim$ 25 ns. This short gate width allows selective detection of only the central slice of the ion sphere. Each ion incident on the MCPs is converted to a pulse of electrons, which yields an optical signal on the phosphor. The image of the scattering distribution at the phosphor screen is captured by the CCD camera and sent to a PC for data processing. Images are typically accumulated over 50,000-100,000 pump-probe cycles.

In order to obtain sufficient information to extract information on electronic angular momentum alignment in the atomic fragments, images were recorded in two different experimental geometries, defined by the polarisations of the photolysis and probe laser beams. In

both cases the photolysis laser was polarised in the plane of the detector, denoted as the ‘horizontal’ plane, or simply ‘H’. The probe laser was either polarised in the same plane, giving the geometry denoted ‘HH’, or parallel to the time-of-flight axis, giving the geometry denoted ‘HV’. These two geometries are illustrated in Figure 2

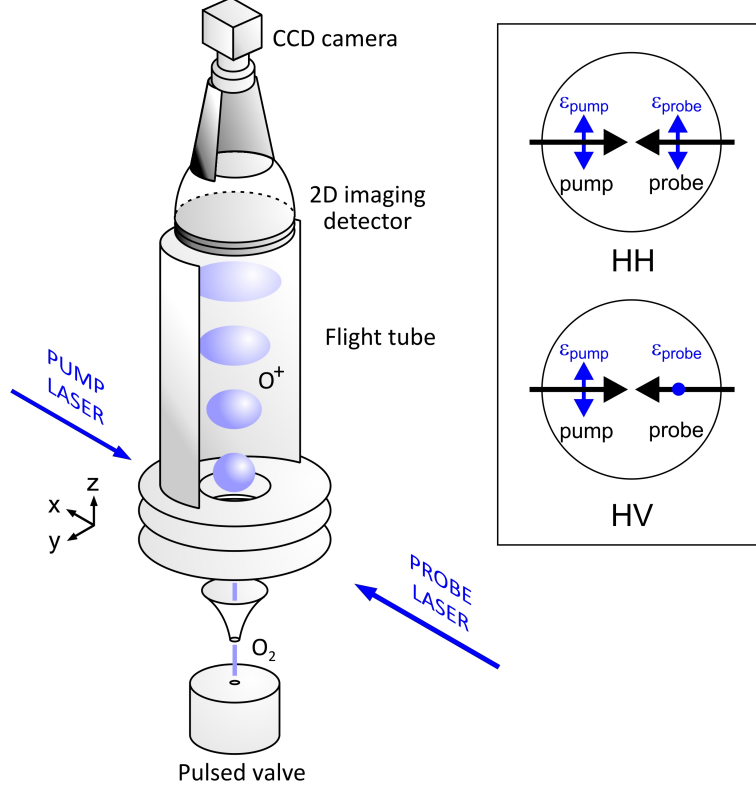


Figure 2: *Schematic of the experimental setup and experimental geometries employed.*

## 2.1 Data analysis

Analysis of the images to extract the spatial anisotropy parameter,  $\beta$ , and the alignment parameters  $a_0^{(2)}(\parallel)$ ,  $a_0^{(2)}(\perp)$ ,  $a_2^{(2)}(\perp)$ , and  $\text{Re}[a_1^{(2)}(\parallel, \perp)]$  is based on fitting Legendre moments of each image to analytical expressions based on the formalism developed by Rakitzis and Zare [11].

The angular distribution  $I(\phi)$  for a sliced velocity-map image may be expanded in Legendre polynomials  $P_n(\cos \phi)$ . For images of  $\text{O}(^3\text{P}_1)$  and  $\text{O}(^3\text{P}_2)$  recorded using the (2+1)REMPI transitions described above, only even terms up to  $n = 4$  are non-zero.



$$I(\phi) = b_0 + b_2 P_2(\cos \phi) + b_4 P_4(\cos \phi) \quad (2)$$

The Legendre moments  $b_0$ ,  $b_2$  and  $b_4$  may be extracted from the experimental data by carrying out the appropriate integrals over the angular coordinate of the image for the ring corresponding to the product of interest.

$$b_n = N \int_0^{2\pi} I(\phi) P_n(\cos \phi) d\phi \quad (3)$$

where  $N$  is a normalisation constant. The Legendre moments extracted from our experimental images as a function of wavelength and experimental geometry are given in Table 5 of Appendix A. As will be explained in more detail below, the moments are normalised such that  $b_0 = 1$ .

An analytical expression for the measured three-dimensional ion signal in a polarised pump-probe experiment was derived in Appendix I of a previous publication [12], and will not be repeated here. To determine expressions for the Legendre moments of sliced images for comparison with the experimental data, we simply restrict the polar angle in the 3D distribution to correspond to velocities lying in the detector plane (this corresponds to setting the angle  $\Omega$  equal to  $\pi/2$  in the notation used in reference [12]), and carry out the equivalent integrals to those given in Equation 3. The resulting expressions for the Legendre moments for the HH and HV geometries employed in the experiments are given below.

$$\begin{aligned} b_0(HH) &= \frac{1}{15} \left[ 15 + s_2 \left\{ 2(\beta + 1)a_0^{(2)}(\parallel) + (\beta - 2)a_0^{(2)}(\perp) + 2\sqrt{6} \left( Re[a_1^{(2)}(\parallel, \perp)] - (\beta - 2)a_2^{(2)}(\perp) \right) \right\} \right] \\ b_2(HH) &= \frac{1}{21} \left[ 21\beta + s_2 \left\{ 11(\beta + 1)a_0^{(2)}(\parallel) - 5(\beta - 2)a_0^{(2)}(\perp) + 2\sqrt{6} \left( Re[a_1^{(2)}(\parallel, \perp)] + 2(\beta - 2)a_2^{(2)}(\perp) \right) \right\} \right] \\ b_4(HH) &= \frac{2}{35} s_2 \left\{ 6(\beta + 1)a_0^{(2)}(\parallel) + 3(\beta - 2)a_0^{(2)}(\perp) - \sqrt{6} \left( 4Re[a_1^{(2)}(\parallel, \perp)] + (\beta - 2)a_2^{(2)}(\perp) \right) \right\} \\ b_0(HV) &= \frac{1}{6} \left[ 6 + s_2 \left\{ -(\beta + 1)a_0^{(2)}(\parallel) + (\beta - 2)a_0^{(2)}(\perp) + \sqrt{6}(\beta - 2)a_2^{(2)}(\perp) \right\} \right] \\ b_2(HV) &= \frac{1}{6} \left[ 6\beta - s_2 \left\{ 2(\beta + 1)a_0^{(2)}(\parallel) + (\beta - 2)a_0^{(2)}(\perp) + \sqrt{6}(\beta - 2)a_2^{(2)}(\perp) \right\} \right] \end{aligned} \quad (4)$$

where  $s_2$  is a REMPI linestrength factor [13]. For the (2+1)REMPI transitions employed

here,  $s_2$  is equal to  $+1$  for detection of  $O(^3P_1)$  photofragments, and  $-1$  for  $O(^3P_2)$  photofragments. Note that the  $b_0$  Legendre moment in the above expressions is essentially an intensity normalisation parameter, and quantifies the extent to which product angular momentum alignment affects the total intensity of an image recorded in a particular experimental geometry. This effect may be dealt with either by making an accurate measurement of the relative intensity of images recorded in the HH and HV geometries, or by normalising the intensity of each image such that  $b_0 = 1$  and rescaling the images within the fitting procedure to account for the differing values of  $b_0$ . In this work we used the latter approach.

For a given wavelength, a Monte-Carlo fitting procedure was used to fit the experimentally determined Legendre moments for the HH and HV detection geometries to the above equations, using  $\beta$ ,  $a_0^{(2)}(\parallel)$ ,  $a_0^{(2)}(\perp)$ ,  $a_2^{(2)}(\perp)$  and  $\text{Re}[a_1^{(2)}(\parallel, \perp)]$  as fitting parameters.

## 2.2 Error analysis

Errors in the image Legendre moments were taken as one standard deviation of the values obtained from several images recorded in the same geometry. The resulting errors in the alignment parameters were determined using a Monte-Carlo procedure. A large number of fits were performed in which values for the experimentally determined Legendre moments were sampled randomly from a Gaussian distribution with a mean and standard deviation matching the experimental data. In each case, the best-fit values for the alignment parameters were determined, and the standard deviation of all of the returned values for a given alignment parameter was taken as the error in that parameter.

## 2.3 Semiclassical calculation of $a_0^{(2)}(\parallel)$ and $a_0^{(2)}(\perp)$

For comparison with the experimentally determined alignment parameters, we have used data from the semiclassical model of van Vroonhoven and Groenenboom [5] to obtain theoretical values for the alignment parameters  $a_0^{(2)}(\parallel)$  and  $a_0^{(2)}(\perp)$  at several wavelengths. Van Vroonhoven and Groenenboom present spatial anisotropy parameters  $\beta$  and molecule frame

alignment tensor moments  $\rho_0^{(2)}$  for each Herzberg state. The alignment tensor moments can be converted into the alignment parameters  $a_0^{(2)}$  of Rakitzis and Zare [11] via the expression [2]

$$a_0^{(2)} = \left[ \frac{(2J-1)(2J+1)(2J+3)}{5J(J+1)} \right]^{1/2} \rho_0^{(2)} \quad (5)$$

The spatial anisotropy parameter for each state may be used to determine the parallel and perpendicular contributions to the alignment for that state. Since a parallel transition corresponds to  $\beta = 2$  and a perpendicular transition to  $\beta = -1$ , the measured value of  $\beta$  is simply  $\beta = 2f_{\parallel} - f_{\perp}$ , where  $f_{\parallel}$  and  $f_{\perp}$  are the fraction of parallel and perpendicular character, and  $f_{\perp} = 1 - f_{\parallel}$ . These equations may be solved to give

$$\begin{aligned} f_{\parallel} &= \frac{1 + \beta}{3} \\ f_{\perp} &= \frac{2 - \beta}{3} \end{aligned} \quad (6)$$

For a given state, we therefore have

$$\begin{aligned} a_0^{(2)}(\parallel) &= f_{\parallel} a_0^{(2)} \\ a_0^{(2)}(\perp) &= f_{\perp} a_0^{(2)} \end{aligned} \quad (7)$$

To determine the overall values of  $a_0^{(2)}(\parallel)$  and  $a_0^{(2)}(\perp)$  for the  $O(^3P_1)$  and  $O(^3P_2)$  photofragments, we need to sum over the contribution from each Herzberg state, taking into account both the excitation branching ratio  $r_n$  into that state and the branching ratio  $b_{n,J}$  from the state into the relevant fine structure component of the  $O(^3P)$  product. The appropriate weighting factors  $w_{n,J}$  for Herzberg state  $n$  and  $O(^3P)$  fine structure state  $J$  are:<sup>2</sup>

---

<sup>2</sup>Note that a similar calculation was carried out by Alexander *et al* for comparison with their experimental data at 222 and 237 nm. However, the branching ratio  $b_{n,J}$  was omitted from their weighting factors for the various Herzberg states. This does not change the calculated values drastically due to the dominant contribution to the dynamics from the  $A^3\Sigma_{u,1}^+$  state.

$$\begin{aligned}
w_{n,J}(\parallel) &= \frac{f_{\parallel,n} r_n b_{n,J}}{\sum_n f_{\parallel,n} r_n b_{n,J}} \\
w_{n,J}(\perp) &= \frac{f_{\perp,n} r_n b_{n,J}}{\sum_n f_{\perp,n} r_n b_{n,J}}
\end{aligned} \tag{8}$$

Both the  $r_n$  and  $b_n$  for each Herzberg state are given in reference [5]. The alignment parameters for a given  $J$  state ( $J = 1, 2$ ) are then

$$\begin{aligned}
a_0^{(2)}(\parallel) &= \sum_n w_{n,J}(\parallel) a_0^{(2)} \\
a_0^{(2)}(\perp) &= \sum_n w_{n,J}(\perp) a_0^{(2)}
\end{aligned} \tag{9}$$

The resulting alignment parameters are included in Figure 3.

## 3 Results and discussion

### 3.1 Spatial anisotropy

Our experimentally determined spatial anisotropy parameters are summarised and compared with previous work in Table 1 and in the top panel of Figure 3. Our measurements are in good agreement with the experiments of Buijsse *et al* [7] and Alexander *et al* [2], and with the theoretical predictions of the semiclassical model developed by van Vroonhoven and Groenenboom [5] over the entire range of wavelengths studied. The predicted values of  $\beta$  for a purely diabatic and purely adiabatic dissociation, also taken from the work of van Vroonhoven and Groenenboom, are included in Figure 3 for comparison, but are not too different from those predicted by the semiclassical model. We see that  $\beta$  stays relatively constant over the wavelength range spanned by the Herzberg continuum, and the results of Bakker and Parker [8] and Brouard *et al* at 193 nm suggest that this behaviour continues down to shorter wavelengths. The good agreement between experiment and theory indicates that the photofragment angular distribution may be understood in terms of well-quantified contributions from the various optically accessible Herzberg states. Excitation to all Herzberg

states except for the  $^3\Sigma_{u,1}^+$  component of the A state occurs via perpendicular transitions from the ground state. However, the transition to the  $A^3\Sigma_{u,1}^+$  state dominates the excitation, accounting for over 70% of the oscillator strength at all wavelengths studied. This excitation has mixed parallel/perpendicular character, and when the contributions from all states are taken into account we find that  $\beta$  is positive. For the  $O(^3P_1)$  products, theory predicts a gradual reduction in  $\beta$  as the dissociation threshold is approached, but no corresponding reduction is apparent for  $O(^3P_2)$ .

Table 1: *Beta parameters recorded for  $O(^3P)$  products of  $O_2$  photolysis at wavelengths within the Herzberg continuum. Results of this work, Buijsse et al [7], Alexander et al [2], Bakker and Parker [8] and Brouard et al [1] are included.*

Author	$\lambda/\text{nm}$	$O(^3P_1)$	$O(^3P_2)$
Brouard	193	$0.63\pm0.05$	$0.63\pm0.05$
Bakker	193	$0.48\pm0.10$	
Buijsse	204	$0.53\pm0.15$	$0.87\pm0.12$
This work	205		$0.72\pm0.09$
This work	216.667	$0.56\pm0.15$	$0.44\pm0.08$
This work	221.667	$0.61\pm0.13$	$0.83\pm0.12$
Alexander	222	$0.51\pm0.10$	$0.55\pm0.10$
Buijsse	226	$0.61\pm0.09$	$0.64\pm0.08$
Buijsse	236	$0.31\pm0.15$	
Alexander	237	$0.31\pm0.15$	$0.50\pm0.10$
This work	237.049		$0.75\pm0.09$
This work	238.5		$0.75\pm0.12$
This work	240 ( $^3P_2 + ^3P_2$ channel)		$0.88\pm0.11$
This work	240 ( $^3P_2 + ^3P_1$ channel)	$0.39\pm0.10$	$0.14\pm0.10$
This work	240 (all $^3P_2$ products)		$0.66\pm0.10$
This work	241 ( $^3P_2 + ^3P_2$ channel)		$0.68\pm0.11$
This work	241 ( $^3P_2 + ^3P_1$ channel)		$0.25\pm0.08$

The fact that significantly different  $\beta$  parameters are observed, and predicted by theory, for the  $O(^3P_1)$  and  $O(^3P_2)$  products is a consequence of the various Herzberg states accessed in the excitation step having different branching ratios into each fine structure state. A

new feature of our velocity-map imaging results is the ability near the dissociation threshold to separate the two channels leading to  $\text{O}(^3\text{P}_2) + \text{O}(^3\text{P}_2)$  and  $\text{O}(^3\text{P}_2) + \text{O}(^3\text{P}_1)$  products, and to determine separate  $\beta$  parameters for the  $\text{O}(^3\text{P}_2)$  products formed in each case. At photolysis wavelengths of 240 and 241 nm, the data presented in Table 1 indicate a much lower  $\beta$  parameter for  $\text{O}(^3\text{P}_2)$  products partnered by  $\text{O}(^3\text{P}_1)$  than for  $\text{O}(^3\text{P}_2)$  partnered by  $\text{O}(^3\text{P}_2)$ . This result is in line with the observed reduction in  $\beta$  near threshold for  $\text{O}(^3\text{P}_1)$  products. At shorter wavelengths it was not possible to resolve the two channels in the  $\text{O}(^3\text{P}_2)$  velocity-map images, so only a total  $\text{O}(^3\text{P}_2)$  spatial anisotropy parameter is determined. The corresponding total  $\text{O}(^3\text{P}_2)$  spatial anisotropy parameter near threshold is in agreement with previous experimental measurements, in which the two dissociation channels were not resolved.

### 3.2 Alignment

The spatial orientation of a quantum mechanical angular momentum vector is determined by the  $M_J$  quantum number, which quantifies the projection of  $\mathbf{J}$  onto a laboratory-frame axis. Alignment of an ensemble of quantum mechanical angular momenta therefore corresponds to a non-equilibrium distribution of  $M_J$  populations. In the context of photodissociation studies, the quantisation axis is usually taken to be the photofragment velocity vector. Various sets of alignment or polarisation parameters are in use for describing photofragment angular momentum polarisation; in the following we will use the alignment parameter formalism of Rakitzis and Zare [11].

For products scattered at a given angle (i.e. for a given angle  $\theta_\epsilon$  between the photolysis polarisation  $\epsilon$  and the photofragment velocity  $\mathbf{v}$ ), the spatial distribution  $D(\theta, \phi; \theta_\epsilon)$  of the product atomic angular momentum may be described in terms of an expansion in modified spherical harmonics  $C_q^k(\theta, \phi)$ , with expansion coefficients  $A_q^{(k)}(\theta_\epsilon)$ .

$$D(\theta, \phi; \theta_\epsilon) = \sum_{k=0}^{2J} \sum_{q=-k}^k A_q^{(k)}(\theta_\epsilon) C_q^k(\theta, \phi) \quad (10)$$

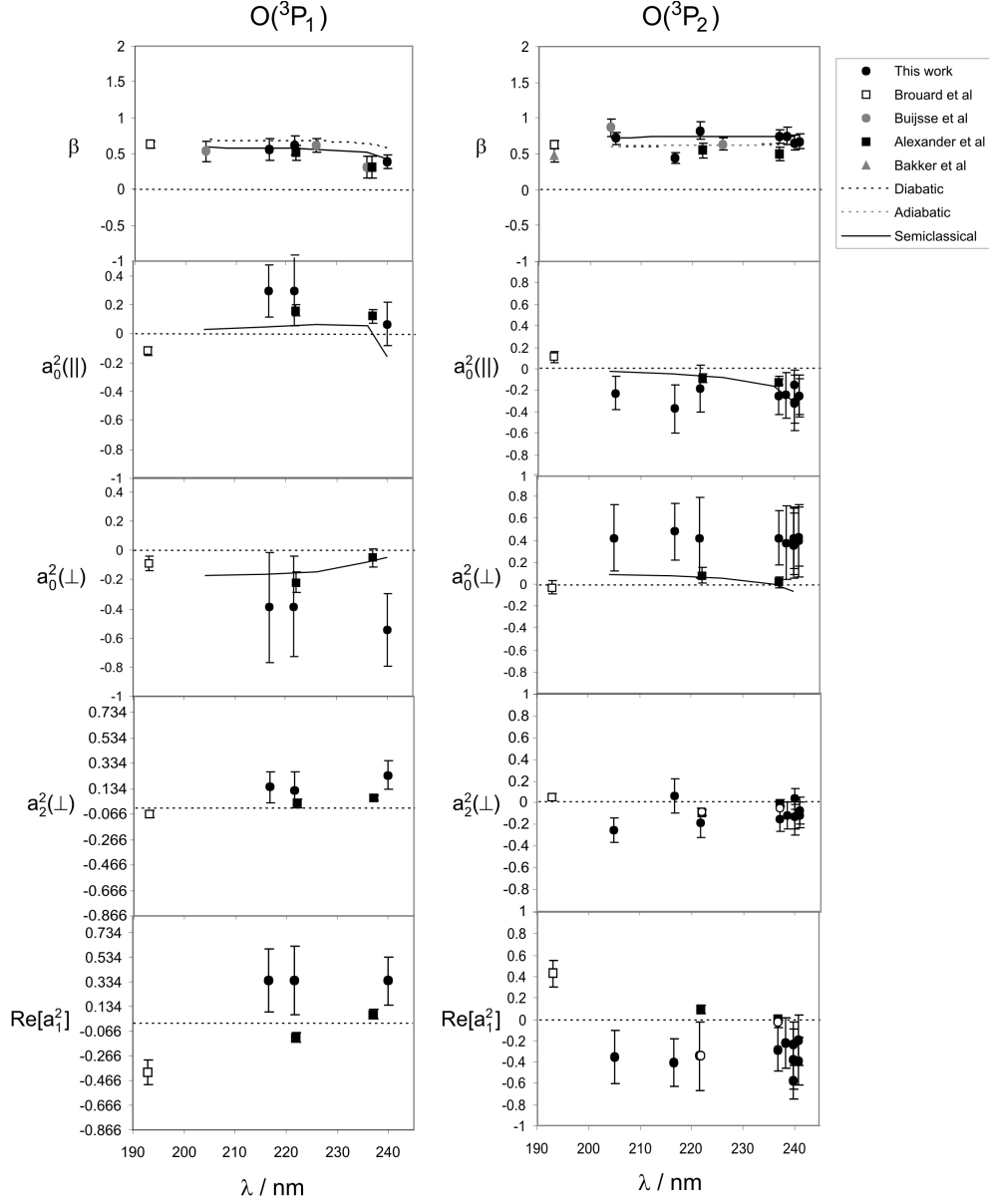


Figure 3: *Beta parameters and alignment parameters recorded for  $O(^3P)$  products of  $O_2$  photolysis at wavelengths within the Herzberg continuum. Results of this work, Buijsse et al [7], Alexander et al [2], and Brouard et al [1] are included, along with theoretical results based on the work of van Vroonhoven and Groenenboom [5]. Note that for the  $O(^3P_2)$  fragments these values are an average over the  $^3P_2+^3P_2$  and  $^3P_2+^3P_1$  channels. Channel-specific  $b$  parameters at 240 and 241 nm are given in Table 1.*

Here,  $\theta$  and  $\phi$  are polar angles in the molecular frame, in which  $z$  is defined to lie parallel to the photofragment recoil velocity vector  $\mathbf{v}$ . The modified spherical harmonics are related

to the standard spherical harmonics by a simple scaling factor:

$$C_q^k(\theta, \phi) = \left( \frac{4\pi}{2k+1} \right)^{1/2} Y_{kq}(\theta, \phi) \quad (11)$$

In order to account for the angular dependence of the  $A_q^{(k)}(\theta_\epsilon)$ , a set of alignment parameters,  $a_q^{(k)}(p)$ , are introduced, where  $p = \parallel, \perp$ .

$$\begin{aligned} A_0^{(k)} &= \frac{(1 + \beta) \cos^2 \theta_\epsilon a_0^{(k)}(\parallel) + (1 - \beta/2) \sin^2 \theta_\epsilon a_0^{(k)}(\perp)}{1 + \beta P_2(\cos \theta_\epsilon)} \\ A_1^{(k)} &= \frac{\sin \theta_\epsilon \cos \theta_\epsilon a_1^{(k)}(\parallel, \perp)}{1 + \beta P_2(\cos \theta_\epsilon)} \\ A_2^{(k)} &= \frac{(1 - \beta/2) \sin^2 \theta_\epsilon a_2^{(k)}(\perp)}{1 + \beta P_2(\cos \theta_\epsilon)} \\ A_q^{(k)} &= (-1)^q A_{-q}^{(k)*} \end{aligned} \quad (12)$$

Our experiments are sensitive to four alignment parameters  $a_0^{(2)}(\parallel)$ ,  $a_0^{(2)}(\perp)$ ,  $a_2^{(2)}(\perp)$ , and  $\text{Re}[a_1^{(2)}(\parallel, \perp)]$ , which have the following interpretations:

- $a_0^{(2)}(\parallel)$  characterises the contribution to photofragment alignment arising from parallel excitations.
- $a_0^{(2)}(\perp)$  and  $a_2^{(2)}(\perp)$  characterise the contribution to photofragment alignment arising from perpendicular excitations.
- $\text{Re}[a_1^{(2)}(\parallel, \perp)]$  represents a contribution to the photofragment alignment arising from the interference between parallel and perpendicular transitions.

In addition to characterising the spatial distribution of  $\mathbf{J}$ , the alignment parameters provide insight into the contributions to the dissociation dynamics from the various Herzberg states, and through their relationship to the density matrix [14] may also be used to determine the atomic  $M_J$  state distributions.

The alignment parameters extracted from our images for the  $\text{O}(^3\text{P}_1)$  and  $\text{O}(^3\text{P}_2)$  photofragments are summarised and compared with the work of Alexander *et al* and Brouard *et al* in Tables 2 and 3. The same data is presented graphically in the lower panels of Figure 3. Note that the vertical scale on the plots corresponds to the physically allowable range of the parameters.



Table 2: *Alignment parameters recorded for  $O(^3P_1)$  products of  $O_2$  photolysis at wavelengths within the Herzberg continuum. Results of this work, Alexander et al [2], and Brouard et al [1] are included.*

$\lambda$	Brouard 193 nm	This work 216.667 nm	This work 221.667 nm	Alexander 222 nm	Alexander 237 nm	This work 240 nm
$\beta$	$0.63 \pm 0.05$	$0.56 \pm 0.15$	$0.61 \pm 0.13$	$0.51 \pm 0.10$	$0.31 \pm 0.15$	$0.39 \pm 0.10$
$a_0^{(2)}(\parallel)$	$-0.12 \pm 0.03$	$0.29 \pm 0.18$	$0.30 \pm 0.24$	$0.16 \pm 0.04$	$0.12 \pm 0.05$	$0.06 \pm 0.15$
$a_0^{(2)}(\perp)$	$-0.09 \pm 0.05$	$-0.39 \pm 0.38$	$-0.38 \pm 0.35$	$-0.22 \pm 0.07$	$-0.05 \pm 0.06$	$-0.54 \pm 0.25$
$a_2^{(2)}(\perp)$	$-0.06 \pm 0.03$	$0.15 \pm 0.12$	$0.13 \pm 0.14$	$0.02 \pm 0.03$	$0.06 \pm 0.02$	$0.24 \pm 0.11$
$Re[a_1^{(2)}(\parallel, \perp)]$	$-0.40 \pm 0.10$	$0.35 \pm 0.26$	$0.35 \pm 0.28$	$-0.12 \pm 0.04$	$0.07 \pm 0.04$	$0.34 \pm 0.19$

Perhaps the first point to note is that in all experimental studies to date, the measured alignment parameters lie well within their physical limits, some way from their limiting values. Alignment resulting from photolysis in the Herzberg continuum is therefore modest. This should be contrasted with the dynamics of  $O_2$  dissociation at shorter wavelengths in the Schumann-Runge continuum [12], in which the  $O(^1D_2)$  products are extremely strongly aligned, being formed almost exclusively in  $M_J = 0$ .

Within experimental error, the  $a_0^{(2)}(\parallel)$  parameters obtained in our measurements are in good agreement with the results of Alexander *et al* for both  $J = 1$  and  $J = 2$  products. They agree in sign with those predicted by the theoretical model, though are somewhat larger in magnitude. Our values for  $a_0^{(2)}(\perp)$  have much greater associated experimental errors than for  $a_0^{(2)}(\parallel)$ , and are in considerably poorer agreement with Alexander *et al*'s results and with the predictions of theory. Though the sign of this parameter agrees with earlier work, our values are considerably larger in magnitude. Our  $a_2^{(2)}(\perp)$  parameters are in good agreement with the earlier measurements, though again perhaps slightly larger in magnitude. The parameter  $Re[a_1^{(2)}(\parallel, \perp)]$  shows the poorest agreement with the earlier experiments, differing in both sign and magnitude. However, our measurements at shorter wavelengths are in good

Table 3: *Alignment parameters recorded for  $O(^3P_2)$  products of  $O_2$  photolysis at wavelengths within the Herzberg continuum. Results of this work, Alexander et al [2], and Brouard et al [1] are included.*

$\lambda$	Brouard 193 nm	This work 205 nm	This work 216.667 nm	This work 221.667 nm	Alexander 222 nm	Alexander 237 nm
$\beta$	$0.63 \pm 0.05$	$0.72 \pm 0.09$	$0.44 \pm 0.08$	$0.83 \pm 0.12$	$0.55 \pm 0.10$	$0.50 \pm 0.10$
$a_0^{(2)}(\parallel)$	$0.11 \pm 0.05$	$-0.23 \pm 0.16$	$-0.37 \pm 0.23$	$-0.19 \pm 0.22$	$-0.09 \pm 0.04$	$-0.13 \pm 0.03$
$a_0^{(2)}(\perp)$	$-0.03 \pm 0.06$	$0.42 \pm 0.30$	$0.48 \pm 0.26$	$0.42 \pm 0.37$	$0.08 \pm 0.07$	$0.02 \pm 0.05$
$a_2^{(2)}(\perp)$	$0.05 \pm 0.03$	$-0.25 \pm 0.11$	$0.06 \pm 0.15$	$-0.18 \pm 0.13$	$-0.09 \pm 0.03$	$0.00 \pm 0.03$
$Re[a_1^{(2)}(\parallel, \perp)]$	$0.42 \pm 0.12$	$-0.36 \pm 0.25$	$-0.41 \pm 0.22$	$-0.35 \pm 0.32$	$0.09 \pm 0.04$	$-0.01 \pm 0.02$
This work 237.049	This work 238.5 nm	This work 240 nm ( $^3P_2 + ^3P_2$ )	This work 240 nm ( $^3P_2 + ^3P_1$ )	This work 222 nm (all $^3P_2$ )	This work 237 nm ( $^3P_2 + ^3P_2$ )	This work 240 nm ( $^3P_2 + ^3P_1$ )
$0.75 \pm 0.09$	$0.75 \pm 0.12$	$0.88 \pm 0.11$	$0.14 \pm 0.10$	$0.66 \pm 0.10$	$0.68 \pm 0.11$	$0.25 \pm 0.08$
$-0.25 \pm 0.18$	$-0.24 \pm 0.21$	$-0.32 \pm 0.19$	$-0.15 \pm 0.14$	$-0.31 \pm 0.26$	$-0.26 \pm 0.20$	$-0.26 \pm 0.17$
$0.42 \pm 0.25$	$0.38 \pm 0.33$	$0.39 \pm 0.31$	$0.35 \pm 0.29$	$0.42 \pm 0.28$	$0.40 \pm 0.33$	$0.43 \pm 0.27$
$-0.15 \pm 0.11$	$-0.12 \pm 0.12$	$-0.13 \pm 0.11$	$0.03 \pm 0.09$	$-0.13 \pm 0.16$	$-0.07 \pm 0.12$	$-0.11 \pm 0.12$
$-0.29 \pm 0.20$	$-0.23 \pm 0.23$	$-0.24 \pm 0.20$	$-0.58 \pm 0.17$	$-0.38 \pm 0.28$	$-0.20 \pm 0.23$	$-0.40 \pm 0.23$

agreement with the semiclassical calculation carried out by Alexander *et al* at 222 nm. This calculation was noted to be at odds with their experimental measurement at this wavelength.

The origins of the discrepancies between the two sets of experimental alignment measurements are not immediately clear. The experiments were carried out using two very different detection techniques, with Alexander *et al* employing time-of-flight profile analysis, in contrast to our sliced velocity-map imaging approach. Each technique has different merits, and it is possible that different systematic errors are introduced in each case. In slice imaging, for example, some uncertainty is introduced into the data analysis by the finite thickness of the measured slice through the velocity distribution. In the published results of Alexander *et al*, while the fits to the data are generally very good, they do appear systematically to underestimate the intensity of the experimental data slightly in some of the experimental geometries employed. Further experimental determinations of  $O(^3P)$  alignment resulting from photolysis of  $O_2$  in the Herzberg continuum would be most welcome in order to resolve

some of the uncertainties in the values of the alignment parameters.

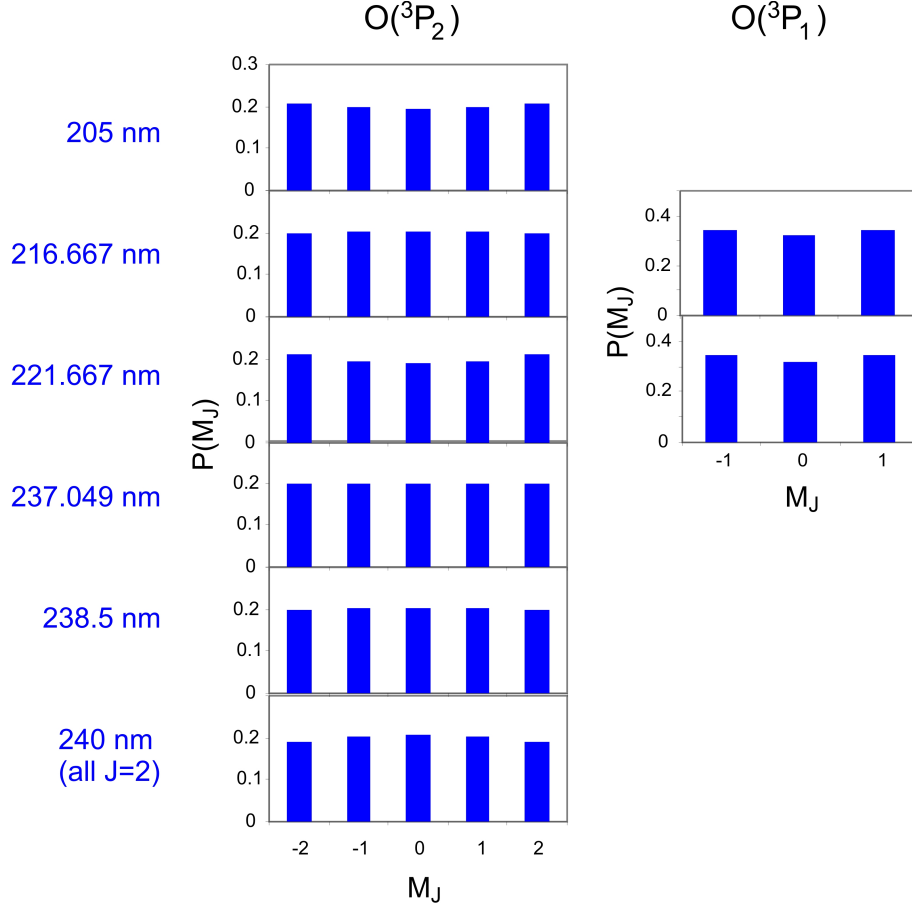


Figure 4:  $M_J$  populations for the  $O(^3P_1)$  and  $O(^3P_2)$  photofragments formed in the photolysis of  $O_2$  at various wavelengths within the Herzberg continuum. All  $J = 2$  populations are averaged over the  $O(^3P_2)+O(^3P_2)$  and  $O(^3P_2) + O(^3P_1)$  channels.

The alignment parameters determined by Brouard *et al* at 193 nm are included in Tables 2 and 3 and Figure 3 for completeness, but are significantly different from values measured at longer wavelengths. For example, the  $a_0^{(2)}(\parallel)$  alignment parameter is found to have the opposite sign when compared with our measurements and those of Alexander *et al* at longer wavelengths. If it is assumed that only the Herzberg states are involved, a negative value for the  $a_0^{(2)}(\parallel)$  parameter for  $J = 1$  products and a positive value for  $J = 2$  products must indicate a strong contribution from some combination of the  $A(^3\Sigma_{u,0}^+)$ ,  $A'(^3\Delta_{u,1})$  and  $A'(^3\Delta_{u,2})$  states. However, unless one or more additional states are involved, or the alignment parameters for the Herzberg states change drastically between 204 nm and 193 nm, this is

at odds with the positive value of  $\beta$ . Considering only the Herzberg states, a positive  $\beta$  can only arise from a strong contribution to the excitation from the  $A^3\Sigma_{u,1}^+$  state, the only state with a parallel component to the transition dipole from the ground state. An alternative explanation for the observed value of  $\beta$  was proposed by Bakker and Parker [8].  $O(^3P_2)$  production at 193 nm is resonance enhanced by the allowed transition to the  $B(^3\Sigma_u^-)(v=4)$  state [8]. This is a pure parallel transition with a positive  $\beta$ , and a mixed transition involving the B state, followed by predissociation via one or more of the Herzberg states could well lead to the observed photofragment alignment. Further theoretical data is required in order to provide decisive conclusions as to the dissociation mechanism at this wavelength.

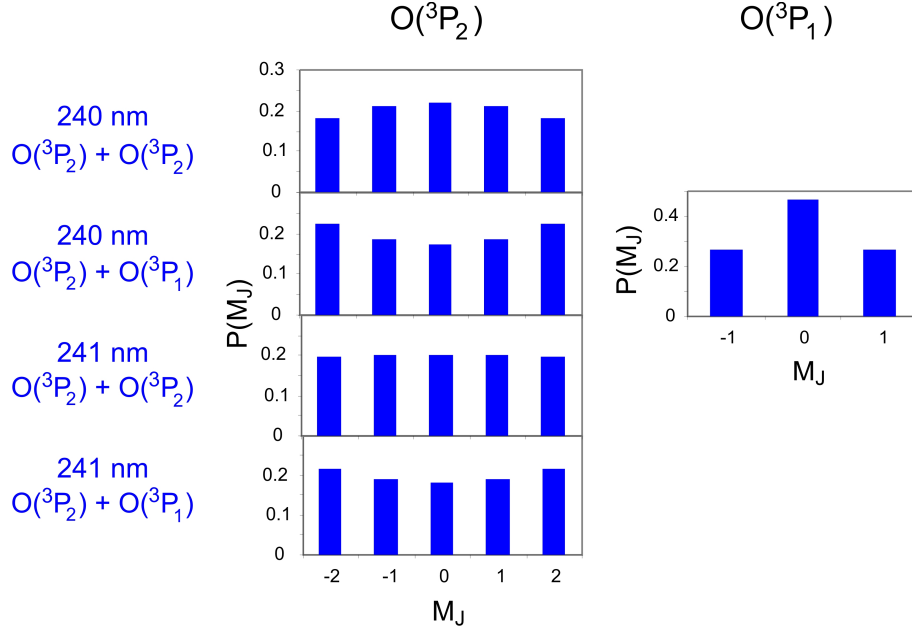


Figure 5:  $M_J$  populations for the  $O(^3P_1)$  and  $O(^3P_2)$  photofragments formed in the photolysis of  $O_2$  near threshold, resolved into  $O(^3P_2)+O(^3P_2)$  and  $O(^3P_2) + O(^3P_1)$  channels.

The measured alignment parameters perhaps become more meaningful when they are used to calculate the  $M_J$  state distributions for the  $O(^3P)$  photofragments. These are simply the diagonal elements of the density matrix [14], which is related to the  $A_q^{(k)}$  of Equation 12 by [11]

$$\rho_{M_J, M'_J} = \sum_{k,q} (-1)^{J+q-M'_J} \frac{(2k+1)[J(J+1)]^{k/2}}{c(k) \langle J || J^{(k)} || J \rangle} \begin{pmatrix} J & k & J \\ -M_J & q & M'_J \end{pmatrix} A_q^{(k)} \quad (13)$$

where the normalisation constant  $c(k)$  takes the values [5]  $c(0) = c(1) = 1$ ;  $c(2) = \sqrt{6}$ ,  $c(3) = \sqrt{5/2}$ ;  $c(4) = \sqrt{35/8}$ , and the reduced matrix elements  $\langle J || J^{(k)} || J \rangle$  are given by the general expression [15]

$$\langle J || J^{(k)} || J \rangle = \left[ \frac{(2J + k + 1)!(k!)^2}{(2J - k)!2^k(2k)!} \right]^{1/2} \quad (14)$$

$M_J$  populations for the  $O(^3P_1)$  and  $O(^3P_1)$  photofragments are shown in Figures 4 and 5. The most striking feature of these distributions is the almost equal population of all  $M_J$  levels across almost all wavelengths studied, for both  $J = 1$  and  $J = 2$  products. Near threshold (see Figure 5), the distributions for  $J = 2$  products become slightly more peaked, at  $M_J = 0$  for fragments partnered by  $J = 2$  coproducts, and at  $M_J = \pm 2$  for those partnered by  $J = 1$  products. For photolysis at 240 nm, we have data for both the  $J = 1$  and  $J = 2$  cofragments. The  $M_J$  distributions for the two cofragments show opposite behaviour, peaking strongly at  $M_J = 0$  for  $J = 1$  products, and less strongly at  $M_J = \pm 2$  for the corresponding  $J = 2$  products. Previous work [16] on  $O(^3P)$  production in the 193 nm photolysis of  $N_2O$  leads us to suggest that this is likely to indicate similar polarisation of the electronic angular momentum  $\mathbf{L}$  for the two fragments, with coupling to the spin yielding different distributions for the total angular momentum  $\mathbf{J}$ . We note that the simple model used to convert between the polarisation of  $\mathbf{J}$  and  $\mathbf{L}$  in the work on  $N_2O$  is not applicable here, as it assumes the diabatic limit, i.e. that the dissociation is too fast for appreciable coupling to occur between  $\mathbf{L}$  and  $\mathbf{S}$  in the exit channel.

## 4 Conclusions

We have presented spatial anisotropy and alignment parameters for the  $O(^3P_1)$  and  $O(^3P_2)$  products of  $O_2$  photolysis at a number of wavelengths spanning the Herzberg continuum, and have compared our results with the previously published experimental values of Buijsse *et al* [7], Alexander *et al* [2], and Brouard *et al* [1] and with the theoretical results of van Vroonhoven and Groenenboom [5]. We have also used our measured alignment parameters to determine  $M_J$  state distributions for each fragment as a function of photolysis wavelength.

There appears to be no strong dependence of the measured alignment on photolysis wavelength. Near threshold, the velocity-map imaging technique employed in our experiments allows us to separate out the two channels leading to  $\text{O}(^3\text{P}_2)+\text{O}(^3\text{P}_1)$  and  $\text{O}(^3\text{P}_2)+\text{O}(^3\text{P}_2)$  products, and we find significantly different alignments in these two cases. All measured  $\beta$  parameters are in good agreement, and while there is less consistency between the various available sets of alignment parameters, the experimental data is now quite extensive and reasonably well converged, and presents an excellent opportunity for comparison with fully quantum theory. Further experimental data would also be welcome in order to address some of the remaining uncertainties in the data.

## Acknowledgements

We thank Gerrit Groenenboom and Peter Rakitzis for helpful discussions during the course of this work. Financial support for the work in Nijmegen was provided by the NWO-FOM managed program Molecular Atmospheric Physics and by the EU ITN Network ICONIC. The work in Oxford was supported by the ERC Starting Independent Researcher grant ImageMS, the EU ITN Network ICONIC, and the EPSRC funded Programme Grant EP/G00224X/1.

## References

- [1] M. Brouard, R. Cireasa, A. P. Clark, F. Quadrini, and C. Vallance, *Phys. Chem. Chem. Phys.*, 2006, **8**, 5549.
- [2] A. J. Alexander, Z. H. Kim, R. N. Zare, *J. Chem. Phys.*, 2003, **118(23)**, 10566.
- [3] T. G. Slanger and R. A. Copeland, *Chem. Rev.* 2003, **103**, 4731.
- [4] M. C. G. N. van Vroonhoven, and G. C. Groenenboom, *J. Chem. Phys.*, 2002, **116**, 1954.
- [5] M. C. G. N. van Vroonhoven, and G. C. Groenenboom, *J. Chem. Phys.*, 2002, **116**, 1965.
- [6] K. Tonokura, N. Shafer, Y. Matsumi, and M. Kawasaki, *J. Chem. Phys.*, 1991, **95(5)**, 3394.
- [7] B. Buijsse, W. J. van der Zande, A. T. J. B. Eippink, D. H. Parker, B. R. Lewis, and S. T. Gibson, *J. Chem. Phys.*, 1998, **108**, 7229.
- [8] B. L. G. Bakker and D. H. Parker, *J. Chem. Phys.*, 2000, **112(9)**, 4037.
- [9] D. L. Huestis, R. A. Copeland, K. Knutsen, T. G. Slanger, R. T. Jongma, M. G. H. Boogaarts, and G. Meijer, *Can. J. Phys.*, 1994, **72**, 1109.
- [10] J. P. England, B. R. Lewis, and S. T. Gibson, *Can. J. Phys.*, 1996, **74**, 185.
- [11] T. P. Rakitzis and R. N. Zare, *J. Chem. Phys.*, 1999, **110(7)**, 3341.
- [12] S-M. Wu, D. Chestakov, G. C. Groenenboom, W. J. van der Zande, D. H. Parker, G. Wu, X. Yang, and C. Vallance, *Mol. Phys.*, 2010, **108(7-9)**, 1145.
- [13] Y. Mo and T. Suzuki, *J. Chem. Phys.*, 1998, **109**, 4691.
- [14] K. Blum, *Density matrix theory and applications, 2nd Ed. (Physics of Atoms and Molecules series)* (Plenum Press, New York, 1996).

- [15] W. R. Simpson, A. J. Orr-Ewing, T. P. Rakitzis, S. A. Kandel, and R. N. Zare, *J. Chem. Phys.*, 1995, **103**(17), 7299.
- [16] M. Brouard, A. P. Clark, C. Vallance, and O. S. Vasyutinskii, *J. Chem. Phys.*, 2003, **119**(2), 771.



## 5 Appendix A: Legendre moments for sliced velocity-map images of $O(^3P_1)$ and $O(^3P_1)$ photofragments.

In the table below we present the Legendre moments,  $b_n$  of our  $O(^3P_2)$  and  $O(^3P_1)$  photofragment slice images as a function of photolysis wavelength and detection geometry. The moments were extracted from the images according to the procedure described in Section 2.1, and have been normalised such that  $b_0 = 1$ .

Table 4: *Legendre moments of  $O(^3P_2)$  and  $O(^3P_1)$  slice images as a function of photolysis wavelength and detection geometry. Note that the  $b_4$  moment for images recorded in the HV geometry should be zero (and generally is within our experimental errors), so these values have been included simply for completeness.*

$\lambda/\text{nm}$	moment	$O(^3P_2)$		$O(^3P_1)$	
		HH	HV	HH	HV
205	$b_2$	$0.56 \pm 0.04$	$0.71 \pm 0.09$		
	$b_4$	$0.05 \pm 0.02$	$0.02 \pm 0.02$		
216.667	$b_2$	$0.56 \pm 0.03$	$0.70 \pm 0.09$	$0.51 \pm 0.03$	$0.45 \pm 0.01$
	$b_4$	$0.05 \pm 0.02$	$-0.03 \pm 0.01$	$0.06 \pm 0.04$	$-0.01 \pm 0.01$
221.661	$b_2$	$0.70 \pm 0.05$	$0.78 \pm 0.01$	$0.58 \pm 0.04$	$0.48 \pm 0.06$
	$b_4$	$0.02 \pm 0.01$	$-0.02 \pm 0.01$	$0.06 \pm 0.01$	$-0.06 \pm 0.06$
237.049	$b_2$	$0.66 \pm 0.04$	$0.64 \pm 0.03$		
	$b_4$	$0.08 \pm 0.03$	$0.03 \pm 0.02$		
238.5	$b_2$	$0.70 \pm 0.01$	$0.64 \pm 0.02$		
	$b_4$	$0.09 \pm 0.01$	$0.01 \pm 0.01$		
240 ( $^3P_2 + ^3P_2$ )	$b_2$	$0.88 \pm 0.02$	$0.74 \pm 0.02$		
	$b_4$	$0.13 \pm 0.01$	$-0.01 \pm 0.02$		
240 ( $^3P_2 + ^3P_1$ )	$b_2$	$0.19 \pm 0.02$	$-0.04 \pm 0.02$	$0.09 \pm 0.02$	$0.39 \pm 0.02$
	$b_4$	$-0.14 \pm 0.03$	$0.08 \pm 0.03$	$0.03 \pm 0.02$	$-0.06 \pm 0.02$
241 ( $^3P_2 + ^3P_2$ )	$b_2$	$0.66 \pm 0.03$	$0.51 \pm 0.04$		
	$b_4$	$0.11 \pm 0.01$	$0.02 \pm 0.04$		
241 ( $^3P_2 + ^3P_1$ )	$b_2$	$0.19 \pm 0.01$	$0.11 \pm 0.01$		
	$b_4$	$0.03 \pm 0.01$	$0.00 \pm 0.01$		